J. Fluid Mech. (1985), *vol.* 153, *pp.* 123–149
Printed in Great Britain

A multiple-scales model of the shock-cell structure of imperfectly expanded supersonic jets

By CHRISTOPHER K. W. TAM, JAY A. JACKSON
Department of Mathematics, Florida State University, Tallahassee, Florida 32306
AND J. M. SEINER
NASA Langley Research Center, Hampton, Virginia 23365

(Received 1 March 1984)

A linear solution modelling the shock-cell structure of an axisymmetric supersonic jet operated at slightly off-design conditions is developed by the method of multiple scales. The model solution takes into account the gradual spatial change of the mean flow in the downstream direction. Turbulence in the mixing layer of the jet has the tendency to smooth out the sharp velocity and density gradients induced by the shocks. To simulate this effect, eddy-viscosity terms are incorporated in the model. Extensive comparisons between the numerical results of the present model and experimental measurements gathered at the NASA Langley Research Center over the Mach number range of $|M_j^2 - M_d^2| \leqslant 1.0$ for underexpanded and overexpanded supersonic jets are carried out. Here M_j is the fully expanded jet Mach number and M_d is the design Mach number of the convergent–divergent nozzle. Very favourable agreement is found. This is especially true for the gross features of the shock cells, including the shock-cell spacings and the pressure amplitudes associated with the shocks. The measured data show that the pressure distributions over the first three or four shock cells usually are rich in fine structures. These fine structures are reproduced by the calculated results. Beyond the first few shock cells the model predicts that the shock-cell structure can be represented by a single Fourier mode of the mean flow. This is confirmed by a careful examination of the experimental data. The appropriate turbulent Reynolds number for shock-cell structure calculation is investigated. It is shown that the best choice is the same as the value found to give the best results for jet mean-flow calculation. The present model is used to explain some of the observed characteristics of broadband shock-associated noise.

1. Introduction

In this paper an analytical model of the quasi-periodic shock-cell structure of an imperfectly expanded supersonic jet is developed using the method of multiple-scales asymptotic expansion. This work represents a part of the authors' efforts to develop a mathematical theory of broadband shock-associated noise of supersonic jets. In a recent paper, Tam & Tanna (1982) suggested that this type of noise is generated by the weak interaction between the quasi-periodic shock cells and the downstream-propagating large turbulence structures in the mixing layer of the jet. The weak interaction produces coherent wave-like disturbances. These disturbances propagate along the jet column in both the upstream and downstream directions. Some of these disturbances have wave components which travel with supersonic phase speeds relative to the ambient condition. These supersonic components, by the wavy wall

analogy, lead immediately to acoustic radiation in the form of Mach waves. In the far field this form of radiated sound becomes the observed shock-associated noise.

To quantify their proposed noise-generation mechanism Tam & Tanna (1982) used simple analytical models to represent the nearly periodic shock cells and the large turbulence structures of the jet. By means of these simple models they derived the shock-associated noise-intensity scaling formula

$$I \propto (M_j^2 - M_d^2)^2, \tag{1.1}$$

where I is the noise intensity, M_j is the fully expanded jet Mach number and M_d is the design Mach number of the convergent–divergent nozzle. In addition, they showed that at a given far-field direction θ the frequency corresponding to the spectral peak of the broadband shock-associated noise is given by

$$f = \frac{u_c}{L(1 - M_c \cos\theta)}, \tag{1.2}$$

where L is the fundamental period or spacing of the weak shock cells, u_c is the convection velocity of the large turbulence structures and M_c is the convection Mach number of the large turbulence structures. It is equal to the ratio of u_c to the ambient speed of sound. The above formulae are applicable to shock-associated noise of supersonic jets operated at slightly off-design conditions. On comparing the predictions of the noise-intensity scaling formula (1.1) and the peak-frequency formula (1.2) with their experimental measurements very favourable agreement was found. The comparison involved data taken at a wide range of jet operating conditions, including hot and cold jets at underexpanded as well as overexpanded pressure ratios. The favourable agreement over such a relatively broad range of jet operating conditions provides strong support for the belief that the proposed mechanism is generally valid.

The vortex-sheet shock-cell model solution used by Tam & Tanna is adequate only as a first approximation. It provides a reasonably good description of the weak shock cells in the region immediately downstream of the nozzle exit where the mixing layer is thin. Experimentally, however, Seiner & Norum (1980) and Seiner & Yu (1981) found from in-flow correlations with the acoustic near field that dominant shock-noise sources are located several shocks beyond the nozzle exit. This observation was also made by Norum & Seiner (1982*a*) using an acoustic source location method. The dominant shock-noise source locations indicated from these experiments was that they lie nearer the end of the plume's potential core. In this region, the mixing layer is quite thick. Therefore, the vortex-sheet shock-cell model cannot be very accurate there. In addition, the vortex-sheet solution implies that the amplitude of each Fourier component of the shock-cell structure remains constant along the entire length of the jet. In reality, due to the spatial change of the mean flow and the effect of turbulence in the mixing layer of the jet the shock-cell strength decreases in the downstream direction, as is evident from the experimental observations reported by Seiner & Norum (1979). The shock-cell strength becomes vanishingly small beyond the transonic point. Thus, in order to be able to predict the characteristics and the absolute intensity of shock-associated noise more accurately, a more realistic shock-cell model solution which takes into account the spatial evolution of the mean flow is needed.

Near the nozzle exit the shock-cell structure is usually rich in fine detail (see the measured data in figures 3–8). However, for the purpose of calculating broadband shock-associated noise it is the gross features of the shock cells in the region close to the end of the potential core of the supersonic jet which are important. In this

paper emphasis will, therefore, be placed not so much on the fine structure of the shock cells but on the overall gross features, such as shock-cell spacings and shock intensity. Experimental observations by Norum & Seiner (1982*b*) and Tam & Tanna (1982) indicate that, beyond the range of jet operating condition defined by

$$|M_j^2 - M_d^2| \leqslant 1.0, \tag{1.3}$$

the shock-associated noise-intensity scaling formula (1.1) no longer applies. The reason for this is the appearance of a Mach disk immediately downstream of the nozzle exit. In this study, the primary concern is hence restricted to the shock-cell structure of weakly imperfectly expanded supersonic jets within the range of fully expanded jet Mach number M_j given by (1.3).

Many attempts have been made in the past to calculate the shock-cell spacings of imperfectly expanded supersonic jets. Earlier works include the vortex-sheet model of Prandtl (1904) and Pack (1950) (see also Tam 1972). Subsequently a number of investigators (e.g. Adamson & Nicholls (1959) and Love (1959)) used inviscid-flow models and the method of characteristics to determine the structural detail of the shock cells close to the nozzle exit. No attempt, however, had been made by these investigators to extend their studies beyond the first two to three shock cells. More recently, Salas (1974) and Dash & Thorpe (1978) developed inviscid Euler codes to calculate the shock cells numerically. Comparisons of these inviscid numerical methods with experimental data as reported by Seiner & Norum (1979, 1980) showed that these models do not provide acceptable results for the prediction of broadband shock-associated noise. The model has since been improved by Dash & Wolf (1983) to include the effect of turbulent mixing through the use of turbulence closure equations. The numerical code was tested by Seiner, Dash & Wolf (1983) and found to provide results that agree reasonably well with experimental measurements. In contrast to the numerical approach of Dash & Wolf the present work is analytical and is based on the method of multiple-scales asymptotic expansion. One important advantage of the present analytical model appears to be that it provides a simple and natural way to investigate the physics of the shock cells and their relationship to broadband shock-associated noise. (This will be elaborated upon later in this paper.) Moreover, it is relatively easy to incorporate the present model into a shock-associated noise theory based on the weak-interaction model of Tam & Tanna (1982).

In §2 of this paper a multiple-scales model of the shock-cell structure of an axisymmetric supersonic jet will be developed. In this model the effect of turbulence in the mixing layer of the jet is simulated by the addition of turbulent eddy-viscosity terms to the momentum equation. Numerical results of this model for both overexpanded and underexpanded jets will be presented in §4. Extensive comparisons with experimental measurements will be made. Very favourable overall agreement is obtained. The agreement is especially good for the gross features of the shock cells near the end of the potential core of the jet. Based on the results of this model a physical explanation as to why broadband shock-associated noise usually contains only a single dominant spectral peak is provided.

2. A multiple-scales shock-cell model

At the nozzle exit of an imperfectly expanded axisymmetric supersonic jet there is a mismatch between the static pressure inside and outside the jet. In order to eliminate this pressure difference, shock waves (or expansion fans in the case of

underexpanded jets) are formed near the nozzle lip. These shocks or expansion fans propagate in the downstream direction. After reflection at the jet axis they eventually propagate to the opposite edge of the supersonic jet boundary. For static jets or jets with subsonic mean flow outside, these disturbances are reflected back as they cannot be transmitted into the outside subsonic environment. To maintain pressure equilibrium at the jet boundary, a shock is reflected back as an expansion wave and vice versa. The successive reflections of the shocks and expansion waves along the jet boundary give rise to the quasi-periodic shock-cell structure.

For supersonic jets operating at slightly off-design conditions the shocks and expansion fans are relatively weak. Prandtl (1904) and later Pack (1950) proposed to model such a weak shock-cell structure as a small-amplitude disturbance superimposed on an otherwise perfectly expanded jet. They chose, for simplicity, to represent the perfectly expanded jet by a column of uniform flow bounded by a vortex sheet. It turns out that, for a given pressure difference Δp at the nozzle exit, the linear boundary-value problem corresponding to the vortex-sheet model can be solved exactly. If p_s denotes the pressure perturbation of the shock-cell structure, $(p_s + p_a)$ being the actual pressure inside the jet, then in cylindrical coordinates (r, θ, x) as shown in figure 1 the solution for p_s is

$$p_s = \sum_{i=1}^{\infty} A_i J_0\left(\frac{2\lambda_i r}{D_j}\right) \cos\left(\frac{2\lambda_i x}{D_j (M_j^2 - 1)^{\frac{1}{2}}}\right), \tag{2.1a}$$

where

$$A_i = 2\Delta p \left(\frac{D}{D_j}\right) \frac{J_1(\lambda_i D/D_j)}{\lambda_i J_1^2(\lambda_i)}, \tag{2.1b}$$

$$J_0(\lambda_i) = 0 \quad (i = 1, 2, 3, \ldots). \tag{2.1c}$$

In (2.1) M_j is the fully expanded jet Mach number, J_0 and J_1 are Bessel functions of orders 0 and 1 respectively, and D_j is the fully expanded jet diameter. It is related to the nozzle-exit diameter D by the condition of conservation of mass flux. An explicit formula relating these two quantities had been given by Tam & Tanna (1982) as

$$\frac{D_j}{D} = \left[\frac{1 + \frac{1}{2}(\gamma - 1) M_j^2}{1 + \frac{1}{2}(\gamma - 1) M_d^2}\right]^{(\gamma+1)/4(\gamma-1)} \left(\frac{M_d}{M_j}\right)^{\frac{1}{2}}. \tag{2.2}$$

In (2.2) γ is the ratio of specific heats and M_d is the nozzle-design Mach number. The magnitude of pressure mismatch Δp is a function of the fully expanded jet Mach number M_j. By using one-dimensional isentropic nozzle-flow relations it is straightforward to derive that

$$\frac{\Delta p}{\rho_j U_j^2} = \frac{1}{\gamma M_j^2} \left\{\left[\frac{1 + \frac{1}{2}(\gamma - 1) M_j^2}{1 + \frac{1}{2}(\gamma - 1) M_d^2}\right]^{\gamma/(\gamma-1)} - 1\right\}, \tag{2.3}$$

where ρ_j and U_j are the fully expanded jet density and velocity respectively.

Equation (2.1) is a slight generalization of the solution obtained by Prandtl and Pack. Here provision has been made for the possibility that the fully expanded jet diameter, D_j (see figure 1), is larger than the physical diameter of the nozzle at its exit D. This situation arises when a jet is operating at an underexpanded condition. For these jets the appropriate boundary conditions at the nozzle exit $x = 0$, as dictated by the physical problem, are

$$\left.\begin{aligned} p_s &= \begin{cases} \Delta p, & r \leqslant \frac{1}{2}D, \\ 0, & \frac{1}{2}D < r \leqslant \frac{1}{2}D_j \end{cases} \\ v_s \text{ (the radial velocity component)} &= 0; \quad r \leqslant \tfrac{1}{2}D_j. \end{aligned}\right\} \tag{2.4}$$

Boundary condition (2.4) has been used to derive solution (2.1).

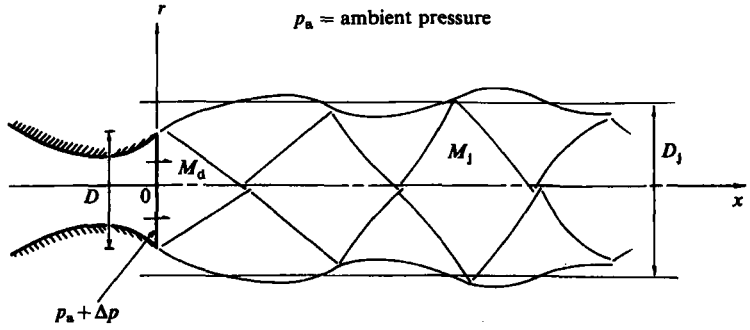

FIGURE 1. Schematic diagram showing the shock-cell system downstream of the nozzle exit of an imperfectly expanded supersonic jet bounded by a vortex sheet.

On the other hand, for overexpanded jets D_j is smaller than D so that instead of (2.4) the appropriate boundary conditions at the nozzle exit $x = 0$ are for purposes of the present analysis given by

$$\left.\begin{aligned} p_s &= \Delta p, \\ v_s &= 0, \end{aligned}\right\} \quad r \leqslant \tfrac{1}{2}D_j. \tag{2.5}$$

Upon using this new boundary condition it is found that the solution is again given by (2.1), provided that the factor D/D_j in (2.1*b*) is replaced by unity.

Physically, solution (2.1) may be regarded as a Fourier decomposition of the quasi-periodic shock-cell structure into the eigenmodes of the mean flow. In the above model the mean flow consists of a vortex-sheet jet. Another way of interpreting this solution is that the jet acts more or less as a waveguide for the pressure disturbances generated by the static pressure mismatch at the nozzle exit. These disturbances propagate downstream along the waveguide. Inside the waveguide these disturbances are decomposed selectively into the intrinsic eigenmodes of the mean flow. By combining these various time-independent eigenmodes linearly one can reconstruct the weak shock-cell structure of the supersonic jet.

Within the jet operating range defined by (1.3) the weak shock (linear) assumption used by Prandtl and Pack appears to be reasonable. This statement is supported by the favourable agreement obtained between the numerical results of this work and experiment to be described in §4. However, the vortex-sheet model has two major drawbacks. First, in a real jet the thickness of the mixing layer, except in the region immediately downstream of the nozzle exit, is not small. The thickness increases in the downstream direction due to the entrainment of ambient fluid until, at the end of the potential core, the jet acquires a fully developed mean-flow profile. Secondly, in a mixing layer of finite thickness, turbulence plays a non-negligible role in reducing the strength of the shock-cell structure. As mentioned before, a completely inviscid shock-cell model could give rather unsatisfactory results.

To develop a realistic shock-cell model, it will be assumed that solution (2.1) is still applicable at the nozzle exit of the jet. However, as each Fourier component propagates downstream it is gradually modified by the mean flow of a real jet. In this paper, to account for this mean-flow effect the measured mean-flow profile of perfectly expanded jets will be used. To simulate the effect of turbulence in the mixing layer of the jet, which is very effective in smoothing out sharp velocity and density gradients associated with shock waves, eddy-viscosity terms will be added to the momentum equation. The measured data of Eggers (1966), Birch & Eggers (1972), Lau, Morris & Fisher (1979) and Lau (1981) indicate that the mean flow of an

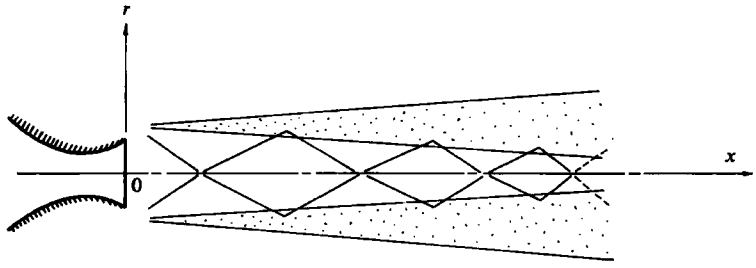

FIGURE 2. Schematic diagram showing the quasi-periodic shock-cell structure in the potential core region of a supersonic jet.

axisymmetric supersonic jet spreads out very slowly in the axial direction. With respect to a cylindrical coordinate system (r, θ, x) centred at the nozzle exit, as shown in figure 2, the mean velocity $\bar{v}$ may be represented analytically in the form

$$\bar{v} = [\epsilon \bar{v}_1(r, s), 0, \bar{u}(r, s)], \tag{2.6}$$

where ϵ is the rate of spread of the mean flow in the core region of the jet and $s = \epsilon x$ is a slow variable. Numerically, ϵ is a small number, typically of the order of 0.05. Here it will be deemed a small parameter and will be used as such later.

The governing equations for the axisymmetric weak shock-cell structure are the time-independent linearized continuity, momentum and energy equations of a compressible fluid. In terms of dimensionless variables, with $R_j = \frac{1}{2}D_j$ (the radius of the fully expanded jet) as the lengthscale, U_j (the fully expanded jet velocity) as the velocity scale and ρ_j (the fully expanded jet density) as the density scale and $\rho_j U_j^2$ as the pressure scale, these equations may be written as

$$\left.\begin{aligned}
&\frac{1}{r}\frac{\partial}{\partial r}(\bar{\rho}vr + \rho\bar{v}r) + \frac{\partial}{\partial x}(\bar{\rho}u + \rho\bar{u}) = 0,\\
&\bar{\rho}\left[\bar{v}\frac{\partial v}{\partial r} + v\frac{\partial \bar{v}}{\partial r} + \bar{u}\frac{\partial v}{\partial x} + u\frac{\partial \bar{v}}{\partial x}\right] = -\frac{\partial p}{\partial r} + \frac{1}{R}\left(\nabla^2 v - \frac{v}{r^2}\right),\\
&\bar{\rho}\left[\bar{v}\frac{\partial u}{\partial r} + v\frac{\partial \bar{u}}{\partial r} + u\frac{\partial \bar{u}}{\partial x} + \bar{u}\frac{\partial u}{\partial x}\right] = -\frac{\partial p}{\partial x} + \frac{1}{R}\nabla^2 u,\\
&\bar{v}\frac{\partial p}{\partial r} + \bar{u}\frac{\partial p}{\partial x} + \frac{1}{M_j^2}\left[\frac{1}{r}\frac{\partial vr}{\partial r} + \frac{\partial u}{\partial x}\right] + \gamma p\left[\frac{1}{r}\frac{\partial \bar{v}r}{\partial r} + \frac{\partial \bar{u}}{\partial x}\right] = 0.
\end{aligned}\right\} \tag{2.7}$$

In (2.7) the quantities with an overbar are those of the fully expanded mean flow. $R = U_j R_j/\nu_t$ is the turbulent Reynolds number and ν_t is the turbulent eddy viscosity.

Advantage will now be taken of the fact that there are two intrinsic but disparate lengthscales in the present problem. One lengthscale is associated with the shock-cell spacing and the other with the much longer slow rate of spread of the mean flow which is characterized by the slow axial variable $s = \epsilon x$. These two lengthscales are very different, so that the well-known method of multiple-scales asymptotic expansion (see Nayfeh 1973) may be used to treat the present problem. In the following it will be assumed that the flow perturbations associated with the ith Fourier component of the shock-cell structure have an asymptotic expansion in ϵ of the form

$$\begin{bmatrix} u \\ v \\ p \end{bmatrix} = \mathrm{Re}\left\{ \sum_{n=0}^{\infty} \epsilon^n A_n(s) \begin{bmatrix} u_n(r, s) \\ v_n(r, s) \\ p_n(r, s) \end{bmatrix} \exp\frac{\mathrm{i}\theta(s)}{\epsilon} \right\}. \tag{2.8}$$

Equation (2.8) represents a two-scale slowly varying wave solution. In this solution $\theta(s)$ is the local phase function. This function describes the dominant periodicity of the shock cells; $A_n(s)$ is the nth-order slowly varying wave-amplitude. (u_n, v_n, p_n) are the nth-order slowly varying shock-cell structure functions. The appropriate boundary conditions are:

(a) the structure functions (u_n, v_n, p_n) must tend to zero as $r \to \infty$, and

(b) they must remain bounded as $r \to 0$.

In the present investigation a turbulent viscosity model (see (2.7)) is used to account for the effect of turbulence in the mixing layer of the jet on the shock-cell structure. Since there is always some uncertainty about such a model and the purpose of including such terms is to smooth out the solution and to account for the dissipation of shock strength by turbulence, to reduce the amount of computation effort required the non-parallel flow effects of these terms are neglected. Actually, these neglected terms are quite small.

Substituting (2.8) into the linearized equation of motion (2.7), and upon partitioning terms according to powers of ϵ, it is straightforward to show that the shock-cell structure functions are governed by a system of first-order differential equations of the form

$$\frac{\mathrm{d}}{\mathrm{d}r}\boldsymbol{Y}_n - \boldsymbol{E}\boldsymbol{Y}_n = \boldsymbol{Q}_n \quad (n = 0, 1, 2, 3, \ldots) \tag{2.9}$$

where $\boldsymbol{Y}_n$ is a column vector with elements $(u_n, \partial u_n/\partial r, v_n, p_n)$. $\boldsymbol{E}$ is a 4×4 matrix whose elements are functions of the mean-flow quantities as indicated below:

$$\boldsymbol{E} = \begin{bmatrix} 0 & 1 & 0 & 0 \\ \mathrm{i}kR\bar{\rho}\bar{u} + k^2 & -\dfrac{1}{r} & R\bar{\rho}\dfrac{\partial \bar{u}}{\partial r} & \mathrm{i}kR \\ -\mathrm{i}k & 0 & -\dfrac{1}{r} & -\mathrm{i}kM_\mathrm{j}^2\bar{u} \\ 0 & \dfrac{-\mathrm{i}k}{R + \mathrm{i}kM_\mathrm{j}^2\bar{u}} & \beta_1 & \beta_2 \end{bmatrix}, \tag{2.10}$$

$$\beta_1 = -\frac{k^2 + \mathrm{i}kR\bar{\rho}\bar{u}}{R + \mathrm{i}kM_\mathrm{j}^2\bar{u}}, \quad \beta_2 = \frac{-\mathrm{i}kM_\mathrm{j}^2\dfrac{\partial \bar{u}}{\partial r}}{R + \mathrm{i}kM_\mathrm{j}^2\bar{u}}$$

and

$$k = \frac{\mathrm{d}\theta(s)}{\mathrm{d}s}. \tag{2.11}$$

The inhomogeneous terms $\boldsymbol{Q}_n$ of (2.9) depend only on the lower-order solutions. In particular, $\boldsymbol{Q}_0 = 0$, so that the lowest-order equation is homogeneous with homogeneous boundary conditions. Therefore, in general, the solution is $\boldsymbol{Y}_0 = 0$. For non-trivial solutions the zeroth-order problem must be treated as an eigenvalue problem. Here k is the eigenvalue. The real part of k has the physical meaning of being the local ith Fourier wavenumber of the quasi-periodic shock cells and the imaginary part gives the spatial rate of decay. The eigenvector describes the radial distribution of the corresponding Fourier component. Since eigenvectors are determined only up to a multiplicative constant, for definiteness we will impose the normalization condition

$$p_0 = 1 \quad \text{at} \quad r = 0 \tag{2.12}$$

on the eigenvectors.

To find the slowly varying wave-amplitude $A_0(s)$ we note that the $n = 1$ order equation of (2.9) is non-homogeneous. Since the homogeneous part of the equation possesses an eigensolution, the non-homogeneous equation will not have a solution unless $\boldsymbol{Q}_1$ is orthogonal to the adjoint eigenvector of the homogeneous problem. It is easy to find that the adjoint eigenvector $\boldsymbol{Z}$ is given by the solution of the following eigenvalue problem:

$$\frac{\mathrm{d}\boldsymbol{Z}}{\mathrm{d}r}+\left(\boldsymbol{E}^{\mathrm{T}}+\frac{1}{r}\boldsymbol{I}\right)\boldsymbol{Z}=0, \tag{2.13a}$$

$$\boldsymbol{Z} \text{ is bounded} \quad \text{as } r\to 0, \tag{2.13b}$$

$$\boldsymbol{Z}\to 0 \quad \text{as } r\to\infty. \tag{2.13c}$$

In (2.13a) $\boldsymbol{E}^{\mathrm{T}}$ is the transpose of $\boldsymbol{E}$. $\boldsymbol{I}$ is the identity matrix. Now if we pre-multiply (2.9) by $r\boldsymbol{Z}^{\mathrm{T}}$ ($\boldsymbol{Z}^{\mathrm{T}}$ is the transpose of $\boldsymbol{Z}$) and integrate over r from 0 to ∞ we find (after integration by parts once and taking into consideration (2.13a)) the following equation:

$$\int_0^\infty r\boldsymbol{Z}^{\mathrm{T}}\boldsymbol{Q}_1\,\mathrm{d}r=0. \tag{2.14}$$

Equation (2.14) is often referred to as the solvability condition. It must be satisfied if (2.9) with $n = 1$ is to have a solution. This solvability condition provides a first-order differential equation for the amplitude function $A_0(s)$. Writing (2.14) out in full we obtain

$$\frac{\mathrm{d}A_0}{\mathrm{d}s}+\frac{h_1(s)}{h_2(s)}A_0=0. \tag{2.15}$$

The functions $h_1(s)$ and $h_2(s)$ are given in Appendix 1. Equation (2.15) can be integrated easily to yield

$$A_0(s)=\frac{2\Delta p}{\rho_{\mathrm{j}}u_{\mathrm{j}}^2}\frac{D}{D_{\mathrm{j}}}\frac{J_1(\lambda_i D/D_{\mathrm{j}})}{\lambda_i J_1^2(\lambda_i)}\exp\left[\mathrm{i}\theta_1(s)\right] \tag{2.16}$$

for underexpanded supersonic jets. For overexpanded jets the ratio D/D_{j} should be replaced by unity. In deriving (2.16) the constant of integration has been evaluated by imposing the initial condition at $s = 0$. At this location it is required that the first term of (2.8) matches the ith Fourier component of the thin vortex-sheet solution, (2.1). The function θ_1 is given by

$$\theta_1=i\int_0^s\frac{h_1(s)}{h_2(s)}\mathrm{d}s;\quad k_1=\frac{\mathrm{d}\theta_1}{\mathrm{d}s}. \tag{2.17}$$

This function represents the first-order non-parallel correction to the locally parallel eigensolution of the linear shock structure. Now, with $A_0(s)$ determined as above, the lowest-order solution of the multiple-scales slowly varying wave solution of (2.8) is found. The higher-order terms can, in principle, be constructed by solving the non-homogeneous equation (2.9) successively. However, they are numerically insignificant and will, therefore, be neglected in this work.

3. Mean-flow profile and numerical method

3.1. *Specification of mean-flow profile and parameters*

In this work the measured mean-flow profiles and characteristic parameters of perfectly expanded supersonic jets obtained by Eggers (1966), Birch & Eggers (1972), Lau *et al.* (1979) and Lau (1981) will be used in the computation of the linear shock-

cell structure. For convenience, the jet will be divided into three regions. They are the core, the transition, and the developed regions. From the extensive measured data it has been found that in all the three regions of the jet the mean-flow velocity profiles can be approximated closely by the following simple functions:

$$\bar{u}(r,s) = \begin{cases} \bar{u}_c, & r \leqslant h, \\ \bar{u}_c \exp\left[-\ln(2)\left(\dfrac{r-h}{b}\right)^2\right], & r > h. \end{cases} \tag{3.1}$$

In (3.1) $\bar{u}_c$ (the centreline velocity of the jet), h (the radius of the uniform core) and b (the half-width of the mixing layer) are functions of the slow variable s.

Closest to the nozzle exit is the core region. In this region, $\bar{u}_c$ of (3.1) is equal to unity. Experimentally, it has been found that the axial momentum flux of a jet is nearly conserved both in the core and in the developed region. This condition of conservation of momentum flux will be used here to provide a functional relation between the two remaining parameters, b and h, of (3.1). In the mixing layer surrounding the uniform core of the jet the mean flow has a similar velocity profile. Because of this similarity, the half-width b may be regarded as a linear function of the axial coordinate. In the present calculation the proportionality constant, which is 1.266 times the inverse of the spreading rate of the mixing layer, will be taken from the data of Birch & Eggers (1972).

Far downstream of the nozzle is the developed region of the jet. In this region h is identically equal to zero. The condition of conservation of axial momentum flux now provides a relation between the jet centreline velocity $\bar{u}_c$ and the half-width b. To complete the specification of the mean-flow profile we will follow the suggestions of Lau *et al.* (1979) and Lau (1981) and adopt the following expression for $\bar{u}_c$:

$$\bar{u}_c = 1 - \exp\left[\alpha\left(1 - \frac{x}{x_c}\right)^{-1}\right]. \tag{3.2}$$

Moreover, their suggested formulae for α and x_c, the length of the uniform core, slightly modified to allow a better fit to Eggers' (1966) data will be used. The modified formula for x_c is

$$\frac{x_c}{D_j} = 4.2 + 1.1 M_j^2 + \Delta\left(\frac{T_j}{T_a}\right), \tag{3.3}$$

$$\Delta\left(\frac{T_j}{T_a}\right) = \begin{cases} 1.1\left(1 - \dfrac{T_j}{T_a}\right) & \left(\dfrac{T_j}{T_a} \leqslant 1\right), \\ \exp\left[-3.2\left(\dfrac{T_j}{T_a} - 1\right)\right] - 1 & \left(\dfrac{T_j}{T_a} > 1\right), \end{cases}$$

where T_j and T_a are the jet and ambient temperature respectively.

The transition region lies between the core and the developed region. In this region the mean velocity profile changes smoothly from one which is characterized by a uniform core to one which is characteristic of self-similar fully developed turbulent flow. The precise location of this region is difficult to ascertain experimentally. Here we will assume that it is centred at $x = x_c$ and extends one-and-a-half jet diameters upstream and downstream. Within the transition region the values of the parameters h, b and $\bar{u}_c$ of (3.1) will each be approximated by a cubic spline curve. The coefficients of the splines are chosen so that these functions as well as their first derivatives in x are continuous throughout the entire jet. In this way a fair degree of smoothness

is achieved. This degree of smoothness ensures that the mean flow indeed varies slowly in the flow direction as required by the method of multiple scales.

With the axial mean-flow profile $\bar{u}$ specified as above, the radial component $\bar{v}$ can be calculated by integrating the mean continuity equation. The mean density $\bar{\rho}$ is determined by the Crocco's relation, which gives

$$\bar{\rho} = \left[\tfrac{1}{2}(\gamma-1)\,\bar{u}(1-\bar{u})\,M_j^2 + \bar{u} + \frac{T_a}{T_j}\left(1+\frac{\gamma-1}{2}M_j^2\right)(1-\bar{u})\right]^{-1}. \tag{3.4}$$

Now the remaining unknown of (2.10) is the turbulent Reynolds number R. The proper choice of R is not obvious. However, it seems reasonable to let R have the same numerical value as has been found suitable for the calculation of the mean flow of a supersonic jet. On following the usual practice in the theories of free turbulent shear flow (see, for example, Schlichting (1960), chapter XXIII; Eggers (1966); Tam (1975)), ν_t is assumed to scale by b, the half-width of the mixing layer, and by u_c as

$$\nu_t = \tfrac{1}{2}Kbu_c. \tag{3.5}$$

In the mean-flow calculation of Tam, the quantity K in (3.5) was allowed to vary slowly over the entire length of the jet. However, over the potential core and the initial part of the developed region the average value of K is approximately equal to $\frac{1}{150}$. This gives a turbulent Reynolds number based on b equal to

$$R_b = \frac{u_c\,b}{\nu_t} \simeq 300. \tag{3.6}$$

For convenience, in all the numerical computations of this paper (except when it is explicitly stated) the value $R_b = 300$ is used.

3.2. *Numerical solution*

With the mean-flow profiles defined as above and the mean density $\bar{\rho}$ determined by the Crocco's relation one can proceed to solve the eigenvalue problem of (2.9). Outside the jet flow, say at $r = h+3.5b$, there is practically no mean flow. Here the matrix $\boldsymbol{E}$ of (2.10) is considerably simplified. This simplification allows the homogeneous equation (2.9) to be solved in closed analytical form in terms of Hankel functions of the first kind. These solutions are given in Appendix 2. At $r = 0$ (2.9) is singular. Two Frobenius series solutions which are bounded at $r \to 0$ can, however, be obtained in a straightforward manner. These series solutions and the exact solution for $r \geqslant h+3.5b$ can now be used to start numerical integrations outward and inward respectively towards the half-velocity point $r = r_{\frac{1}{2}} \equiv h+b$. At $r = r_{\frac{1}{2}}$ the two solutions so calculated must be joined together to obtain continuity. This, in general, cannot be done unless k takes on special values, namely the eigenvalues. Thus this joining condition provides an iterative criterion for the computation of the eigenvalue k and the corresponding eigenvector. With the eigenvalue and eigenvector calculated and the adjoint eigenvector computed in a similar manner, the numerical value of h_1 and h_2 of (2.17) may be evaluated readily. The ratio of these two quantities gives the non-parallel flow correction to the locally parallel flow results.

4. Comparison of numerical results with experiment

Extensive pressure measurements obtained at the NASA Langley Research Center of the shock-cell structures of imperfectly expanded supersonic jets are available in the comprehensive data report of Norum & Seiner (1982*b*). A careful study of these

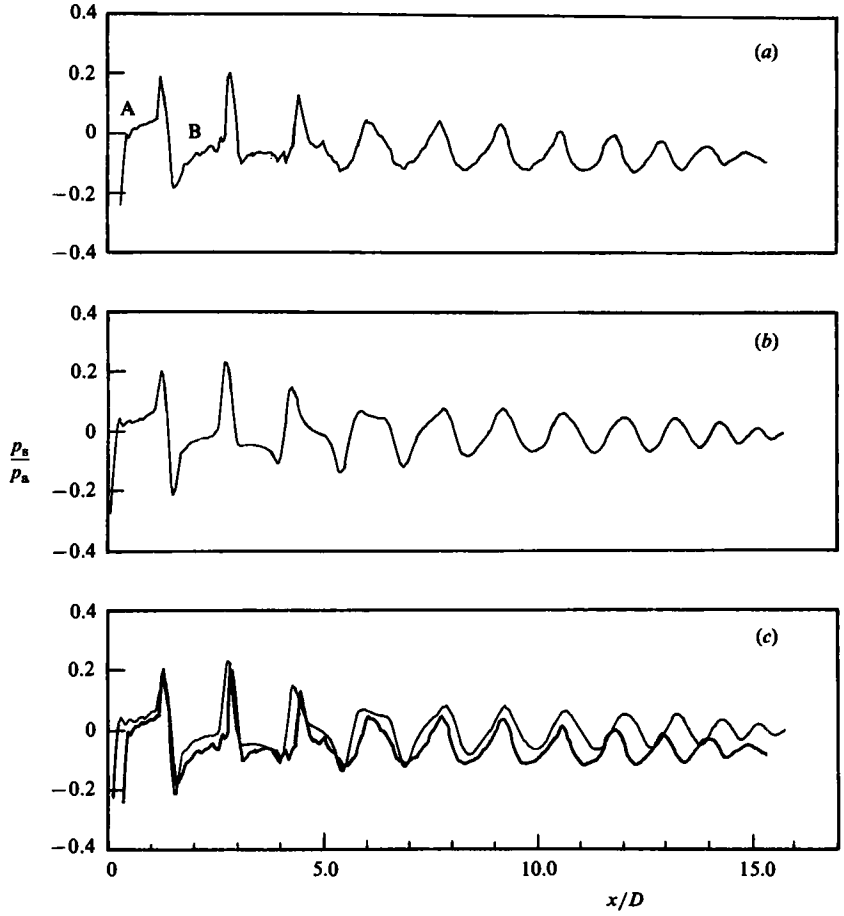

FIGURE 3. Axial pressure distribution at $r/D = 0.38$, $M_j = 1.82$, $M_d = 2.0$: (*a*) measured (Norum & Seiner 1982*b*); (*b*) calculated; (*c*) superposition of measured and calculated pressure distributions.

data reveals that the shock cells are rich in fine details. This is especially true in the region immediately downstream of the nozzle exit – say over the first three to four shock cells. Since the primary objective of this work is to provide a suitable shock-cell model for shock-associated noise calculation, in comparing calculated results with experiments, therefore, attention will be focused principally on the gross features of the shock cells, such as the shock spacings and amplitudes. The fine details of the shock structure are not known to play any important role in noise generation. In addition, the measurements indicate that the mean static pressure inside the jets is not truly constant in accordance with the boundary-layer approximation. Near the end of the potential core and beyond, the mean static pressure is consistently somewhat below the ambient value. This small discrepancy, which is inherent in the mean-flow assumption, should be borne in mind when comparing the measured results with calculations.

4.1. *Comparison of axial pressure distribution*

The present model is linear. As such, the calculated results are expected to agree better with measurements if the shocks are weak or when $|M_j^2 - M_d^2|$ is small. Thus it seems appropriate to begin comparing the theoretical results of the present model with

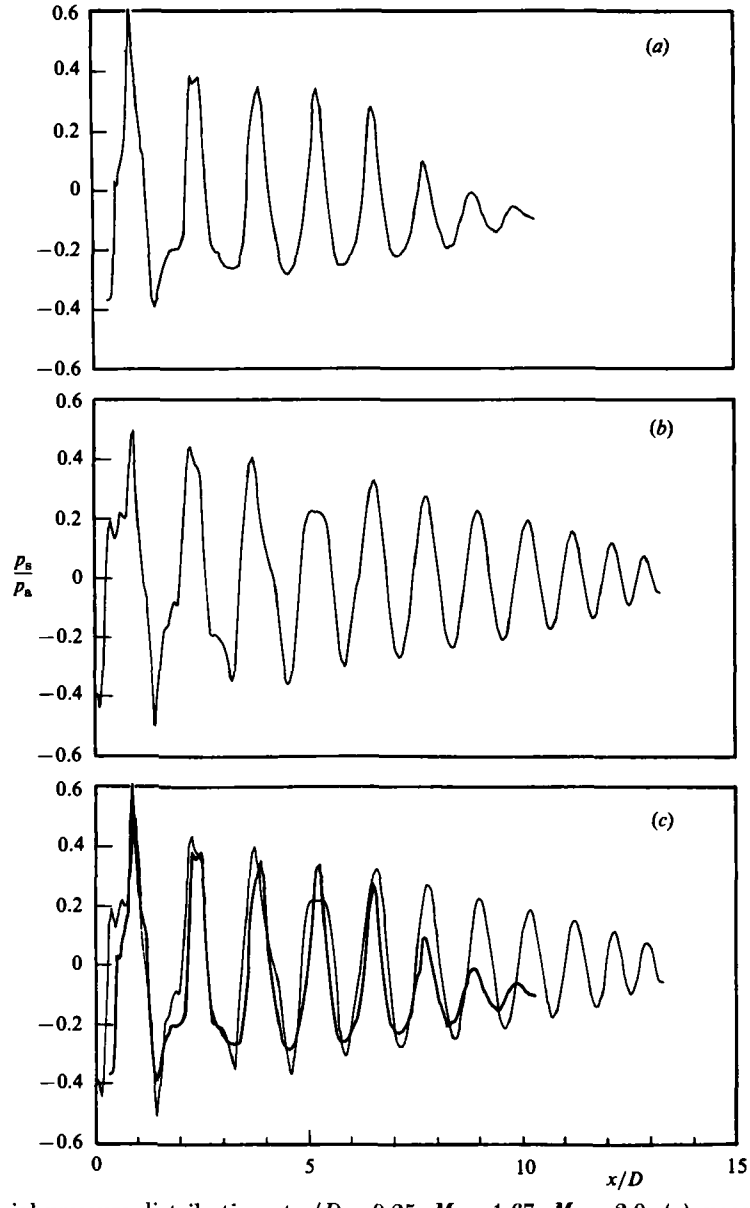

FIGURE 4. Axial pressure distribution at $r/D = 0.25$, $M_j = 1.67$, $M_d = 2.0$: (*a*) measured (Norum & Seiner 1982*b*); (*b*) calculated; (*c*) superposition of measured and calculated pressure distributions.

experiments by first considering those cases for which the jets are operated at very slightly off-design conditions. Throughout this section the experimental data are taken from the report of Norum & Seiner (1982*b*). Figure 3 shows a comparison of the measured and calculated axial pressure distribution for a weak shock-cell structure at a radial distance of $r/D = 0.38$. The jet is operated at a fully expanded Mach number M_j of 1.82 and is issued from a convergent–divergent nozzle of design Mach number M_d of 2.0. The measured pressure difference p_s normalized by the ambient pressure p_a as a function of downstream distance is given in figure 3(*a*). The calculated values are shown in figure 3(*b*). Figure 3(*c*) is a superposition of the

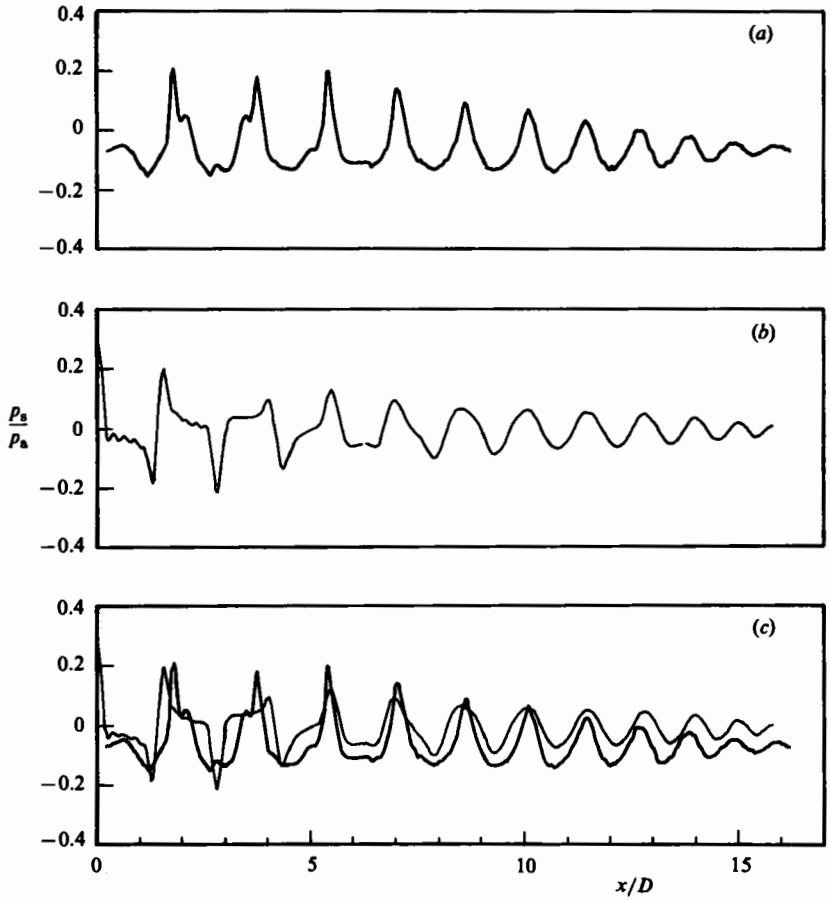

FIGURE 5. Axial pressure distribution at $r/D = 0.45$, $M_j = 1.67$, $M_d = 1.5$: (*a*) measured (Norum & Seiner 1982*b*); (*b*) calculated; (*c*) superposition of measured and calculated pressure distributions.

calculated and measured pressure distribution. As can be seen, there is very favourable overall agreement between the measured and calculated pressure distributions over the full length of the supersonic region of the jet. Both the shock-cell spacings and pressure amplitudes agree extremely well. Within the region of the first four shock cells the calculated pressure distribution exhibits many fine structures, such as those minor oscillations at 'A' and 'B'. They appear to match those of the measured curve. Although there is some slight difference quantitatively, considering the richness of the details and the simplicity of the model the agreement must be regarded as remarkable. Figure 4 shows a similar comparison but for a more severe off-design condition with $M_j = 1.67$, $M_d = 2.0$. The overall agreement in terms of shock-cell spacing and amplitude is again quite favourable. The only exception is that the measured data appear to decay abruptly after the fifth shock cell. Further supporting measurements have shown that for jets exhibiting strong resonance behaviour, i.e. screech, the jet plume shock-structure decays rapidly beyond the potential core. The data of figure 4 refer to such a condition, and it is to be expected that large differences will occur between prediction and measurements due to the nature of the present time mean formulation. The numerical method of Dash & Wolf (1983) also exhibits similar difficulties in predicting the resonant supersonic jet (see

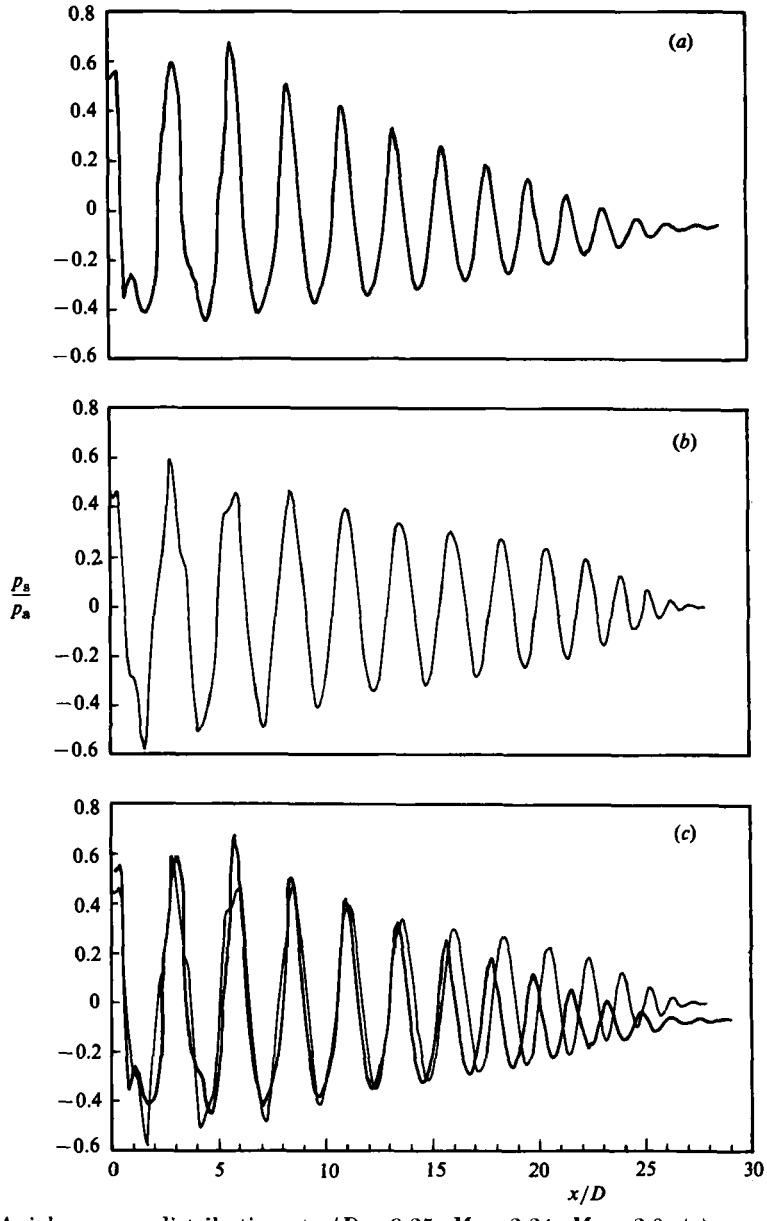

FIGURE 6. Axial pressure distribution at $r/D = 0.25$, $M_j = 2.24$, $M_d = 2.0$: (*a*) measured (Norum & Seiner 1982*b*); (*b*) calculated; (*c*) superposition of measured and calculated pressure distributions.

Seiner, Dash & Wolf 1983). The comparison in figure 4 does, however, show that a good qualitative agreement exists between theory and experiment for the first several shocks, the fine details being represented very well. The above two cases involve overexpanded jets. Figure 5 shows a comparison between theory and experiment for the case of an underexpanded jet with $M_j = 1.67$ and $M_d = 1.5$. The overall agreement between the measured and calculated values of the spacings and amplitudes of 12 shock cells, as can be seen readily in figure 5(*c*), is again quite good. In the first three shock cells the measured data in figure 5(*a*) contain several minor peaks and

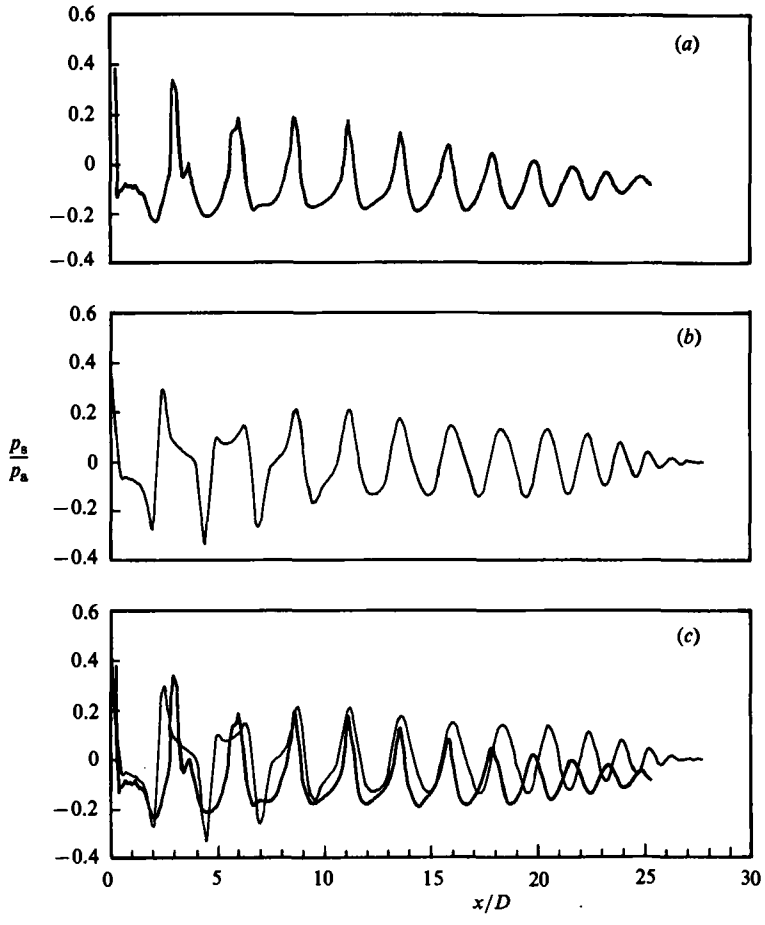

FIGURE 7. Axial pressure distribution at $r/D = 0.45$, $M_j = 2.24$, $M_d = 2.0$: (*a*) measured (Norum & Seiner 1982*b*); (*b*) calculated; (*c*) superposition of measured and calculated pressure distributions.

irregularities as in the case of overexpanded jets. The calculated pressure distribution in figure 5(*b*) appears to reproduce these peculiar features. Although they are somewhat wider the absolute amplitudes of these irregularities appear to have been calculated correctly.

To test whether the present linear shock-cell model is valid at the upper limit of the range of off-design conditions defined by (1.3), a series of comparisons between measured data and calculated results for the case $M_j = 2.24$, $M_d = 2.0$ ($M_j^2 - M_d^2 = 1.0$) at three radial positions will now be made. Figure 6(*a*) and (*b*) shows the measured and calculated pressure distribution at a radial location $r/D = 0.25$ from the jet axis. Figure 6(*c*) is a superposition of these two figures to allow for an easy overall comparison. There are fourteen identifiable shock cells in the measurement. They are quite accurately reproduced in the calculation. The slight difference between the measured and calculated curves beginning with the eighth shock cell is mainly due to the fact (already pointed out) that the mean static pressure of the jet is somewhat below the ambient value, whereas in the calculation, for simplicity, it has been assumed to be equal. Figure 7 shows a comparison of the measured and calculated results at a radial location farther away from the jet axis. At $r/D = 0.45$ the shock cells are well inside the mixing layer of the jet. Figure 7(*c*), which is a

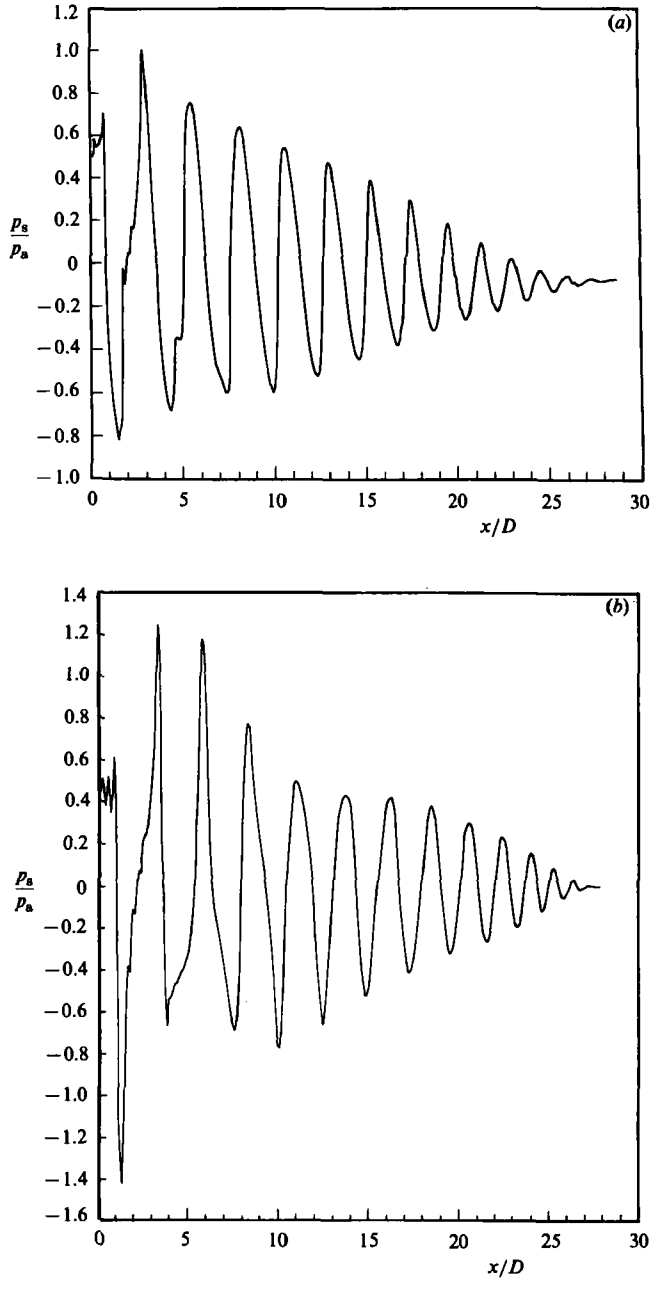

FIGURES 8(*a*) and (*b*). For caption see facing page.

superposition of the measured and calculated pressure distributions, shows that there is again very favourable overall agreement between experiment and theory. In the first shock cell of the measured data (figure 7*a*) there are numerous fine-scale spatial oscillations in the pressure distribution. These oscillations are accurately predicted in the calculation, as can be seen in figure 7(*b*). Over the second to the fourth shock cells the theoretical curve qualitatively reproduces the fine spatial features of the measurement. However, quantitatively, the width is slightly inaccurate. Figures 8(*a–c*) show the measured and computed pressure distributions along the

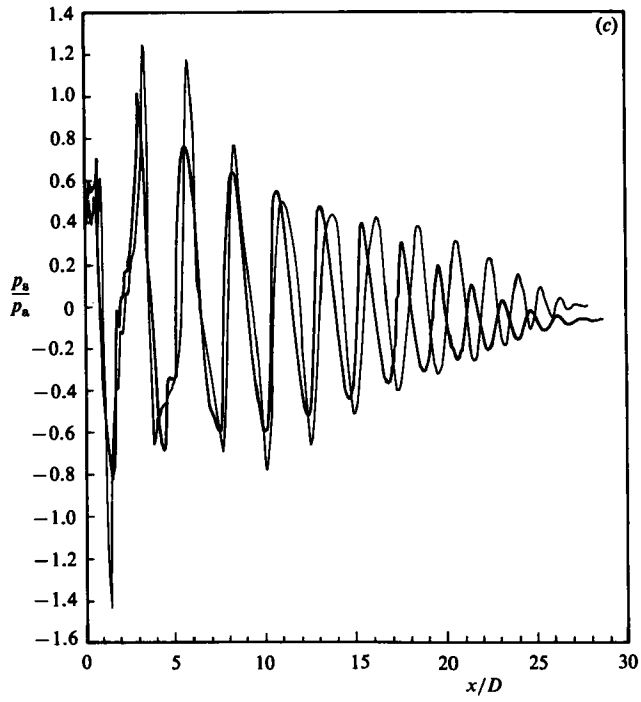

FIGURE 8. Axial pressure distribution $r/D = 0.0$, $M_j = 2.24$, $M_d = 2.0$: (*a*) measured (Norum & Seiner 1982*b*); (*b*) calculated; (*c*) superposition of measured and calculated pressure distributions.

centreline of the jet. There is again good overall agreement between the two. The good agreement is comparable to those of figures 6 and 7. The fine structures which appear in the first two shock cells of the measured data are once more qualitatively reproduced by the calculation. The theoretical results shown in figures 6–8 indicate that the present analysis properly accounts for the radial decay of shock strength, which is a natural feature of jet plume dynamics. In summary, based on the very favourable comparisons between measured and calculated results at the three radial locations $r/D = 0.0, 0.25, 0.45$, as shown in figures 6, 7 and 8, it is possible to conclude that the present multiple-scales model can provide quite accurate prediction of the gross properties of the shock-cell structure even at the upper limit of the jet operating range defined by (1.3). This is true for both axial and radial pressure distributions.

4.2. *The roles of the fundamental and higher-order modes*

Having demonstrated that the present model can provide fairly accurate prediction of the shock-cell structure within the intended range of jet operating conditions, we will now use this model to examine some underlying physics of the shock-cell structure that have a direct bearing on the observed characteristics of shock-associated noise. In figures 3–8 the calculated axial pressure distributions are made up of a linear combination of the first seven Fourier components or modes of the shock-cell model. Obviously different modes play different roles in defining the shock-cell structure. Some are, of course, more important than others. Figure 9 shows the spatial distribution of the first six Fourier modes which make up the theoretical pressure distribution of figure 8(*b*). As can be seen easily, the wavelengths and initial amplitudes of the higher-order modes decrease rapidly as the mode number increases. In addition, their amplitudes diminish to zero over an increasingly shorter distance.

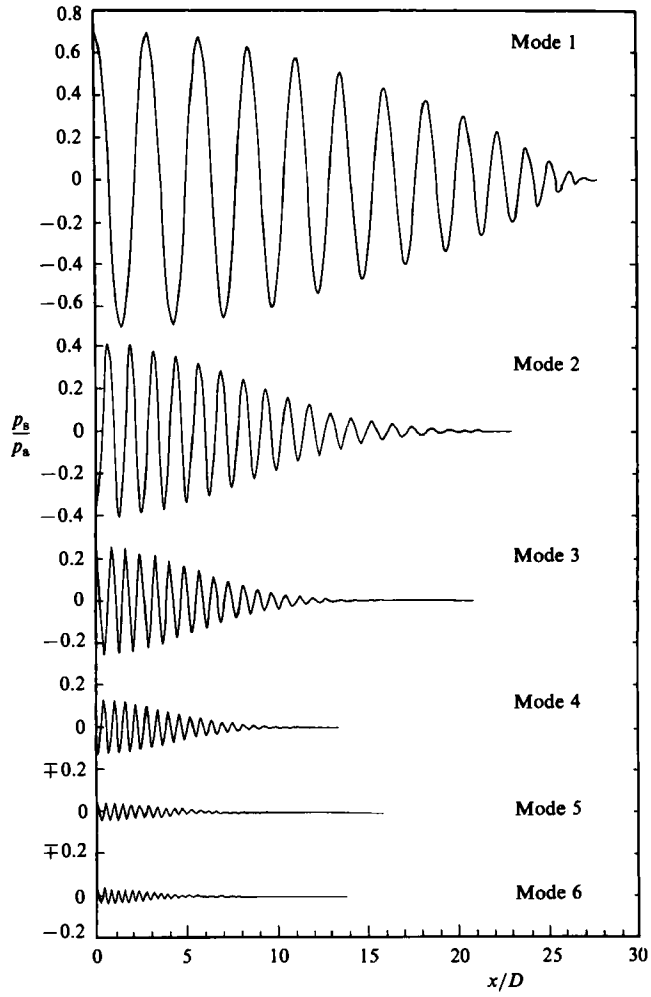

FIGURE 9. Axial distribution of the first six Fourier modes which make up the pressure distribution of figure 8(*b*).

These observations indicated clearly that the higher-order modes are important only in contributing to the fine structures of the beginning shock cells. Further, beyond the first four or five shock cells the shock-cell structure can be approximated reasonably well by using only the first or the fundamental mode.

To demonstrate the relationship between the higher-order modes and the fine structures of the shock cells, the six modes of figure 9 are recombined in two different ways. They are shown in figure 10. Figure 10(*a*) is just the first mode. Figure 10(*b*) is a combination of the first three modes. Notice that the addition of the second and third modes introduces some fine structures in the first three shock cells. Figure 10(*c*) is a combination of the first six modes. As can be seen easily in this figure, the addition of the next three modes refines the fine structures further. With seven modes, these fine structures are fully developed as shown in figure 8(*b*). Figure 11 gives another example illustrating this point. The jet operating conditions for these calculated results are identical to those of figure 3. Figure 11(*a*) consists of the first mode alone. Figure 11(*b*) is obtained by adding on to figure 11(*a*) two additional modes. Again,

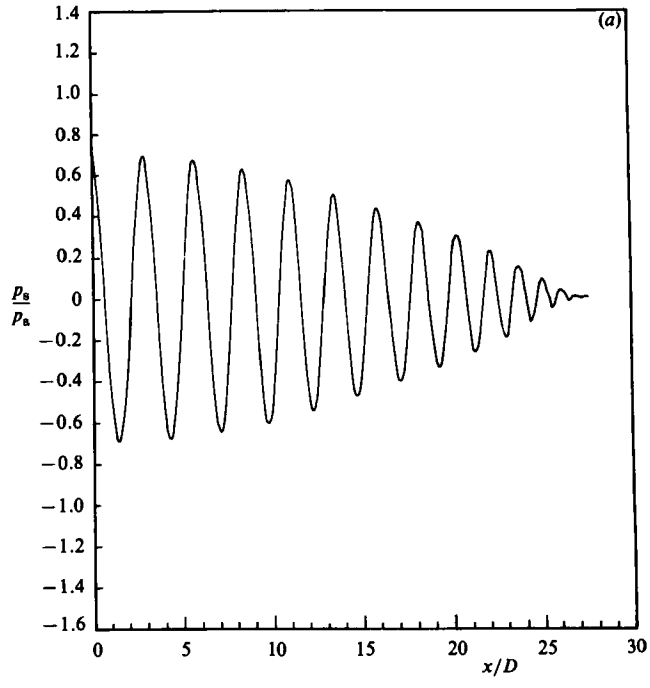

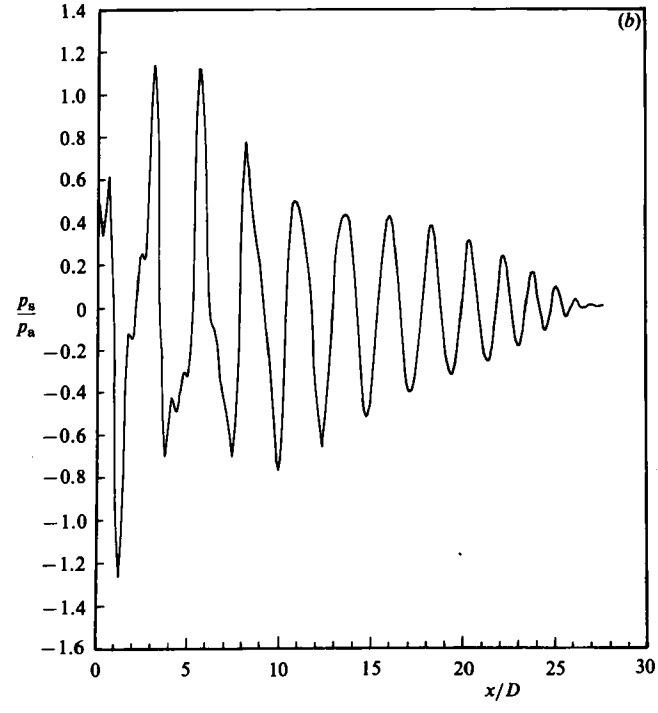

FIGURES 10(*a*) and (*b*). For caption see p. 142.

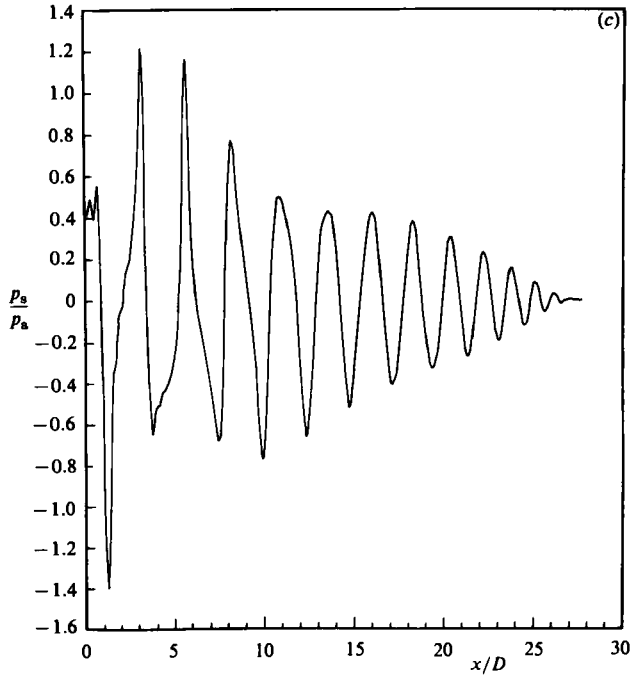

FIGURE 10. (*a*) Axial pressure distribution of the fundamental mode alone. $r/D = 0.0$, $M_j = 2.24$, $M_d = 2.0$. (*b*) Combined axial pressure distribution of the first three Fourier modes. $r/D = 0.0$, $M_j = 2.24$, $M_d = 2.0$. (*c*) Combined axial pressure distribution of the first six Fourier modes. $r/D = 0.0$, $M_j = 2.24$, $M_d = 2.0$.

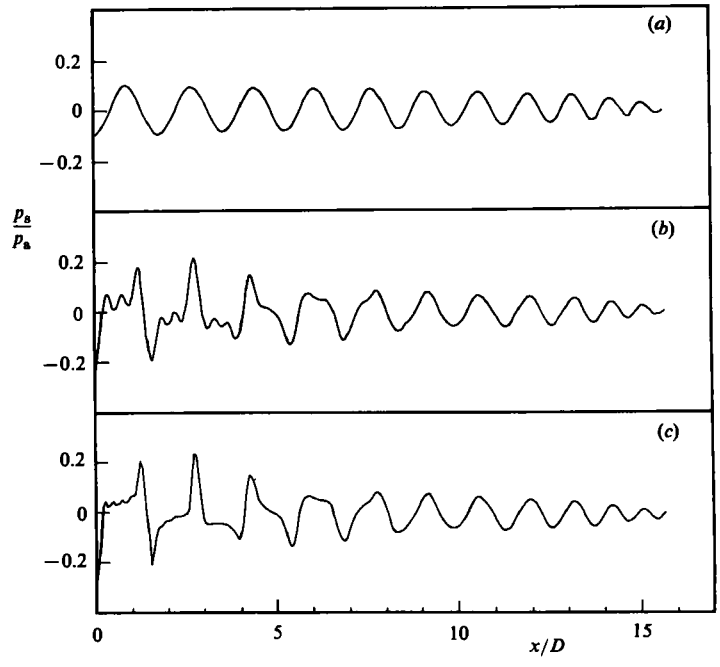

FIGURE 11. Axial pressure distribution $r/D = 0.38$, $M_j = 1.82$, $M_d = 2.0$: (*a*) fundamental mode only; (*b*) first three modes; (*c*) first six modes.

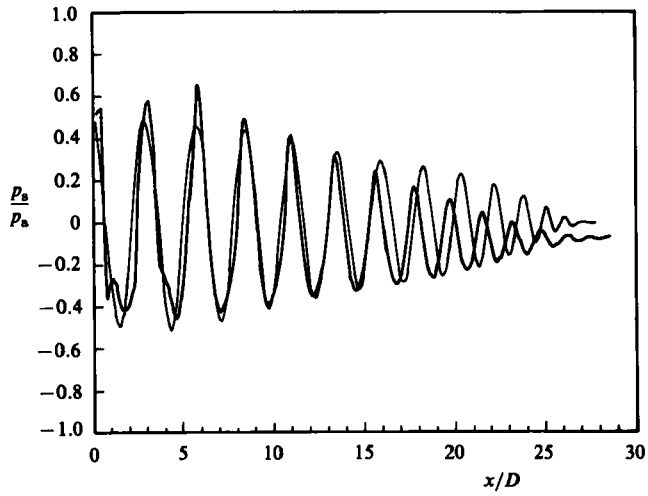

FIGURE 12. Comparison between measured pressure distribution at $r/D = 0.25$, $M_j = 2.24$, $M_d = 2.0$ (dark curve, Norum & Seiner 1982*b*) and calculated pressure distribution of the first mode (lighter curve).

these additional modes produce fine structures in the first four shock cells. In figure 11 (*c*) three more modes are added. Clearly with six modes the fine details of the shock cells are now well established.

By examining figures 10 and 11 it should be evident that beyond the first four or five shock cells only the first (or the fundamental) mode contributes significantly to the shock-cell pressure amplitude. To provide further evidence to substantiate this conclusion, comparisons between measured data and the calculated pressure distribution corresponding to the first mode alone for two additional cases will now be presented. Figure 12 shows the case with $M_j = 2.24$, $M_d = 2.0$ and $r/D = 0.25$. Figure 13 is for a choked jet with $M_d = 1.0$. The fully expanded jet Mach number is 1.166. It is clear from these figures that beyond the first few shock cells there is favourable overall agreement between the calculated results and experiments (assuming the mean pressure difference is subtracted out). In fact, the agreement is reasonably good even for the first few shock cells.

4.3. *The effect of turbulent Reynolds number*

In all the numerical results reported so far the turbulent Reynolds number, R_b, based on the half-width of the jet mixing layer, has been set equal to 300. As was discussed in §3 this value was chosen because it was an appropriate value for mean-flow calculation for shock-free jets. However, it must be pointed out that there is really no *a priori* reason that this same value is also suitable for shock-cell structure calculations.

Let us now examine the effect of turbulent Reynolds number on the calculated axial pressure distribution. For this purpose, we will study the consequence of varying the turbulent Reynolds number on the first mode of the shock-cell structure for a jet operating at $M_j = 2.24$, $M_d = 2.0$ and at $r/D = 0$. The experimental measurements corresponding to this case can be found in figure 8. Figure 14 shows the calculated results at turbulent Reynolds numbers of 150, 300 and 500. It is evident from this figure that the variation of turbulent Reynolds number has very little effect on the spacings or wavelengths of the shock cells. However, there is a significant effect on

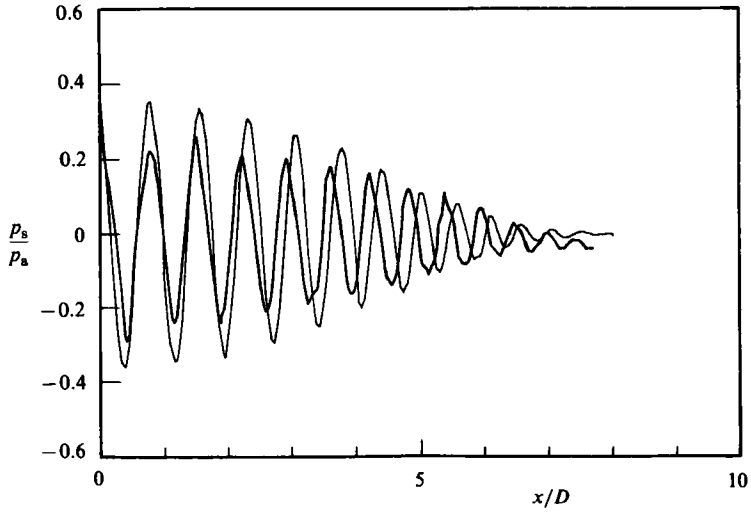

FIGURE 13. Comparison between measured pressure distribution at $r/D = 0.0$, $M_j = 1.166$, $M_d = 1.0$ (dark curve, Norum & Seiner 1982*b*) and calculated pressure distribution of the first mode (lighter curve).

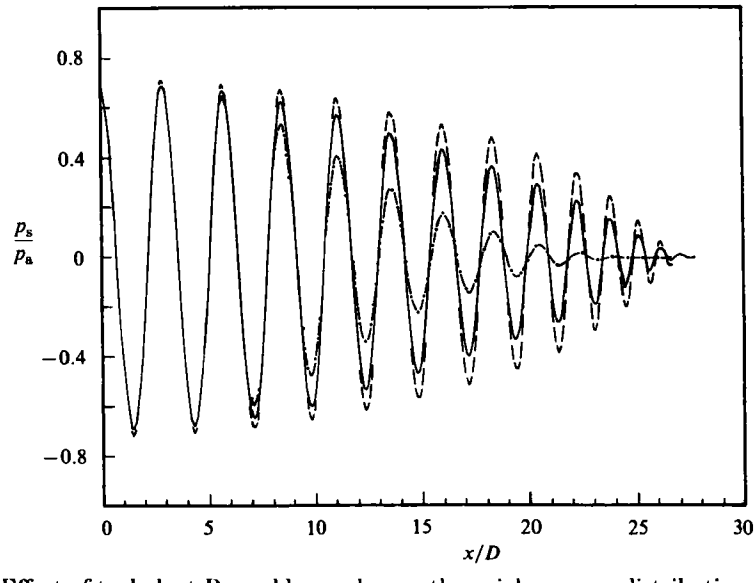

FIGURE 14. Effect of turbulent Reynolds number on the axial pressure distribution of shock cells. $r/D = 0.0$, $M_j = 2.24$, $M_d = 2.0$. First mode: —·—, $R = 150$; ——, $R = 300$; – – –, $R = 500$.

the pressure amplitude. At $R_b = 150$ the shock-cell amplitude decreases very rapidly after the fourth cell. On the other hand, at $R_b = 500$ the calculated pressure amplitude remains quite large until more or less the transonic point of the jet. A systematic analysis indicates that setting $R_b = 300$ produces nearly the best overall agreement with experiment as can be seen in figure 8(*c*). It is interesting to recall that this is the same as the best value for mean-flow calculation. The coincidence here is, of course, not completely accidental. As has been shown, within the jet operating

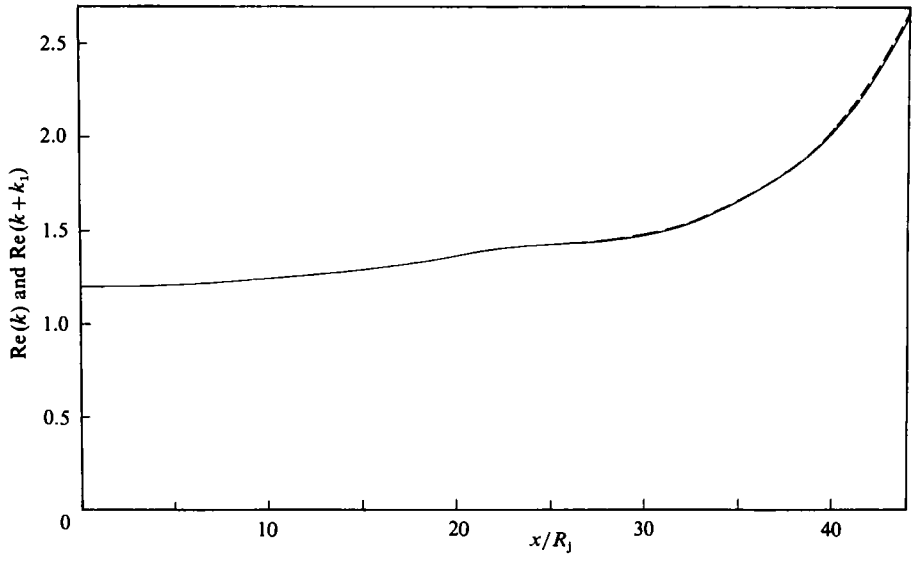

FIGURE 15. Comparison of wavenumber with and without non-parallel flow correction. ——, $\mathrm{Re}\,(k)$; – – –, $\mathrm{Re}\,(k+k_1)$; $M_j = 2.24$, $T_r/T_a = 1.0$, first mode.

range defined by (1.3) the shocks of the shock-cell structure are weak. This is particularly true beyond the fourth or fifth shock cells where the shock structure is essentially represented by only the first Fourier mode. Thus the 'shocks' are not really shocks with sharp discontinuities as have been generally taken for granted. The associated gradients are sufficiently smooth that the effect of turbulence on these shocks is more or less the same as that on the mean flow. With this understanding it is, therefore, not surprising that the same turbulent Reynolds number should be used in both instances.

4.4. *Non-parallel flow correction*

In the multiple-scales shock-cell structure model developed in §2, the calculations are to be performed in two basic steps. The first step is to determine the local eigenvalues and eigenvectors as if the mean flow is parallel. Upon the completion of this step the amplitude function $A_0(s)$ is calculated using the solvability condition. The spatial variation of $A_0(s)$ or, more generally, $\theta_1(s)$ is referred to as the non-parallel flow correction. It is well known that, although the total solution is unique, the magnitude of A_0 or θ_1 by itself is affected by the normalization condition imposed on the eigenvectors. In this work the normalization condition (2.12) has been used throughout. To assess the importance of non-parallel flow correction, let us compare the calculated wavelength and decay rate of the fundamental (or the first) mode with and without this correction. A typical case is shown in figures 15 and 16. In figure 15 the wavenumber, $\mathrm{Re}\,(k)$ (locally parallel flow), and $\mathrm{Re}\,(k+k_1)$ (with non-parallel flow correction) are plotted as a function of downstream distance. Since the two curves are practically identical the non-parallel flow effect on wavenumbers is for all intents and purposes negligible. Figure 16 shows the corresponding results for the decay rate $\mathrm{Im}\,(k)$ and $\mathrm{Im}\,(k+k_1)$. Over the core and the transition region of the jet the non-parallel flow correction is small. Only well inside the developed region of the jet is this effect

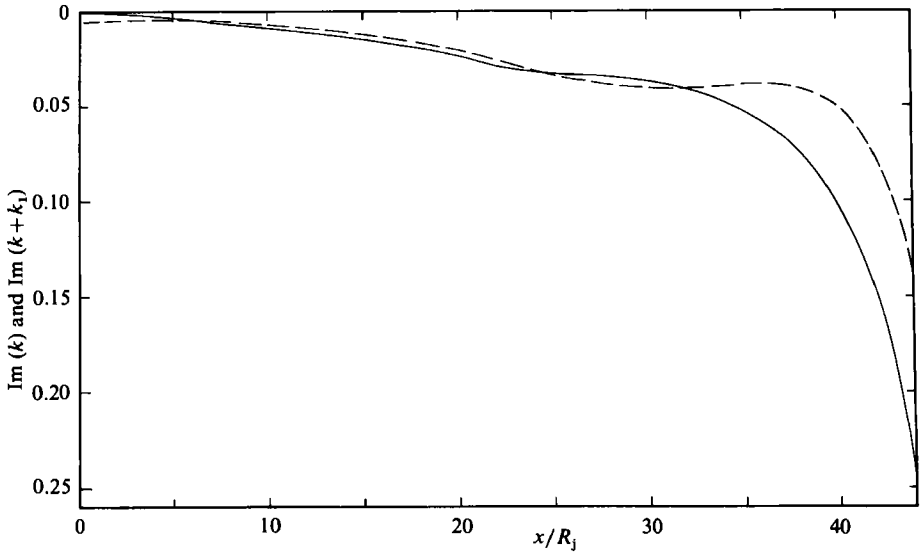

FIGURE 16. Comparison of spatial rate of decay with and without non-parallel flow correction. ——, Im (k); – – –, Im $(k+k_1)$; $M_j = 2.24$, $T_r/T_a = 1.0$, first mode.

significant. To determine computationally the non-parallel flow correction requires far more effort than is necessary to calculate the basic eigenvalue and eigenvectors of the locally parallel flow solutions. Now with normalization condition (2.12) the non-parallel flow effect appears to be not important over most parts of the shock-cell structure. This finding permits one to calculate the shock-cell structure using the simpler locally parallel approximation alone. In this way a good deal of non-essential computation may be avoided.

5. Concluding remarks

In this paper a linear shock-cell model is developed for supersonic jets operated at slightly off-design conditions. The model accounts for the slow variation of the mean flow in the downstream direction and the effect of turbulence in the mixing layer of the jet. As a result of the spatial change of the mean flow the shock-cell spacing decreases gradually in the axial direction. From the nozzle exit to approximately the end of the potential core where it is known (see Norum & Seiner 1982*a*; and Seiner & Yu 1981) that the dominant sources of broadband shock-associated noise are located, the change in shock-cell spacing is not negligible. Figure 17 shows a comparison of the predicted peak frequencies of broadband shock-associated noise as a function of observation angle θ according to (1.2) using the shock-cell spacing at the end of the potential core of the jet calculated by the present model and by the vortex-sheet model. In the calculation, u_c has been taken to be equal to $0.7u_j$ following the experimental observations of Harper-Bourne & Fisher (1973) and Seiner & Yu (1981). From figure 17 it is seen that the peak frequencies predicted by the present model agree better with the measurements of Tam & Tanna (1982) over all angles. This better agreement should lend confidence in using the present model as a starting-point for the development of a mathematical theory of shock-associated noise.

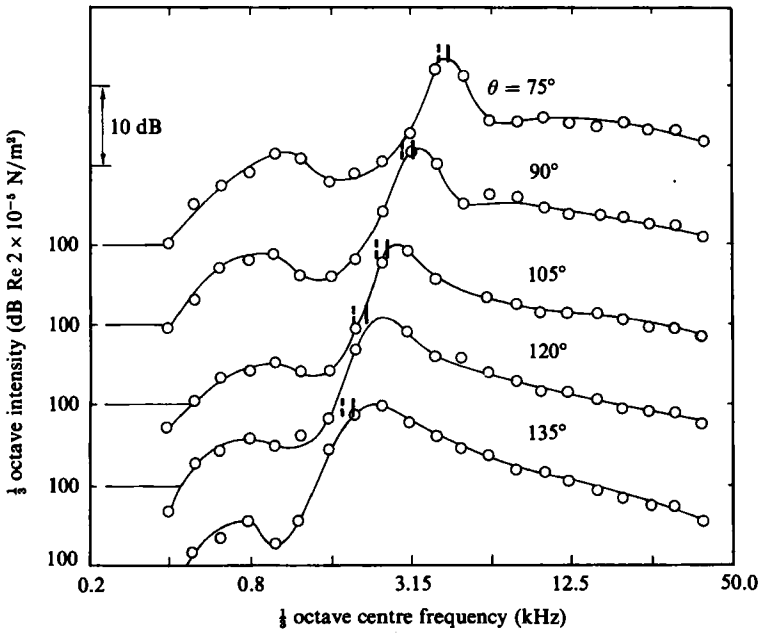

FIGURE 17. Variation of peak frequency with angle, $M_j = 1.925$, $M_d = 1.67$, $T_r/T_a = 1.0$. ○, experiment (Tam & Tanna 1982), calculated peak frequency: ¦ , vortex sheet model; | , present model.

The experimental data shown in figure 17 are typical of all shock-associated noise spectra. At a given direction θ the noise spectrum is dominated by a single peak. A satisfactory explanation of why there is a single dominant peak does not appear to have been given in the literature. In fact, according to the vortex-sheet shock-cell model (see Tam & Tanna 1982), there should be an array of spectral peaks. Each peak is supposed to be generated by the interaction of the downstream-propagating large turbulence structures in the mixing layer of the jet and a Fourier component of the quasi-periodic shock cells. Now the reason why only a single prominent peak is observed appears to lie in what was found in §4.2. That is, after four or five shock cells the shock-cell structure consists mainly of the fundamental mode. At the nozzle exit the large turbulence structures are weak. They grow in amplitude as they propagate downstream. In the region near the end of the potential core of the jet where they grow to sufficiently large amplitudes to interact with the shock-cell structure to generate intense sound waves, the shock-cell structure effectively consists of one single Fourier component. For this reason the observed broadband noise spectrum has only one dominant peak and the peak frequency can be predicted by using the wavelength of the fundamental mode of the shock-cell structure.

Two of the authors (C.K.W.T. & J.A.J.) wish to acknowledge the support of NASA Lewis Research Center under Grant NAG3-182.

Appendix 1

The functions $h_1(s)$ and $h_2(s)$ of (2.15) are given by

$$h_1 = \int_0^\infty \Bigg[R\left(\bar{\rho}\bar{v}_1 \frac{\partial u_0}{\partial r} + \bar{\rho}\frac{\partial \bar{u}}{\partial s}u_0 + \bar{\rho}\bar{u}\frac{\partial u_0}{\partial s} + \frac{\partial p_0}{\partial s}\right) Z_2$$
$$-\left(\frac{\partial u_0}{\partial s} + M_j^2 \bar{v}_1 \frac{\partial p_0}{\partial r} + M_j^2 \bar{u}\frac{\partial p_0}{\partial s}\right) Z_3$$
$$-\left(\bar{\rho}\bar{v}_1 \frac{\partial v_0}{\partial r} + \bar{\rho}\frac{\partial \bar{v}_1}{\partial r}v_0 + \bar{\rho}\bar{u}\frac{\partial v_0}{\partial s}\right)\frac{Z_4}{(1+ikM_j^2\bar{u}/R)}\Bigg] r\,\mathrm{d}r,$$

$$h_2 = \int_0^\infty \left[R(\bar{\rho}\bar{u}u_0 + p_0) Z_2 - (u_0 + M_j^2 \bar{u} p_0) Z_3 - \frac{\bar{\rho}\bar{u}v_0 Z_4}{1+ikM_j^2\bar{u}/R}\right] r\,\mathrm{d}r,$$

where Z_i is the ith element of the adjoint eigenvector $\boldsymbol{Z}$.

Appendix 2

For large r, two linearly independent solutions of (2.9) are

$$\boldsymbol{Y}_0 = \begin{bmatrix} H_0^{(1)}(ikr) \\ -ikH_1^{(1)}(ikr) \\ -H_1^{(1)}(ikr) \\ 0 \end{bmatrix} \quad \text{and} \quad \begin{bmatrix} rH_1^{(1)}(ikr) \\ ikrH_0^{(1)}(ikr) \\ -rH_2^{(1)}(ikr) \\ (2/R)H_0^{(1)}(ikr) \end{bmatrix},$$

where $H_n^{(1)}$ is the nth-order Hankel function of the first kind.

In the uniform core of the jet where $\bar{u} = u_j$, two linearly independent solutions of (2.9) can also be found. They are ($r \leqslant h$)

$$\boldsymbol{Y}_0 = \begin{bmatrix} -\left(1+\frac{ikM_j^2}{R}\right) J_0\left(k\left\{\frac{M_j^2}{1+ikM_j^2/R}-1\right\}^{\frac{1}{2}} r\right) \\ \left(1+\frac{ikM_j^2}{R}\right) k\left\{\frac{M_j^2}{1+ikM_j^2/R}-1\right\}^{\frac{1}{2}} J_1\left(k\left\{\frac{M_j^2}{1+ikM_j^2/R}-1\right\}^{\frac{1}{2}} r\right) \\ -i\left(1+\frac{ikM_j^2}{R}\right)\left\{\frac{M_j^2}{1+ikM_j^2/R}-1\right\}^{\frac{1}{2}} J_1\left(k\left\{\frac{M_j^2}{1+ikM_j^2/R}-1\right\}^{\frac{1}{2}} r\right) \\ J_0\left(k\left\{\frac{M_j^2}{1+ikM_j^2/R}-1\right\}^{\frac{1}{2}} r\right) \end{bmatrix}$$

and

$$\begin{bmatrix} (ikR+k^2)^{\frac{1}{2}} J_0(i(ikR+k^2)^{\frac{1}{2}} r) \\ -i(ikR+k^2) J_1(i(ikR+k^2)^{\frac{1}{2}} r) \\ -kJ_1(i(ikR+k^2)^{\frac{1}{2}} r) \\ 0 \end{bmatrix}.$$

REFERENCES

Adamson, T. C. & Nicholls, J. A. 1959 On the structure of jets from highly underexpanded nozzles into still air. *J. Aero. Sci.* **26**, 16–24.

Birch, S. F. & Eggers, J. M. 1972 A critical review of the experimental data for developed turbulent free shear layers. *NASA SP*-321 vol. 1.

DASH, S. M. & THORPE, R. D. 1978 A new shock-capturing/shock fitting computational model for analyzing supersonic inviscid flow. *ARAP Rep. No.* 366.

DASH, S. M. & WOLF, D. E. 1983 Shock-capturing parabolized Navier–Stokes model for the analysis of turbulent underexpanded jets. *AIAA paper* 83-704.

EGGERS, J. M. 1966 Velocity profile and eddy viscosity distributions downstream of a Mach 2.2 nozzle exhausting to quiescent air. *NASA TN* D-3601.

HARPER-BOURNE, M. & FISHER, M. J. 1973 The noise from shock waves in supersonic jets. *AGARD Conf. Proc.* 131.

LAU, J. C. 1981 Effects of exit Mach number and temperature on mean flow and turbulence characteristics in round jets. *J. Fluid Mech.* **105**, 193–218.

LAU, J. C., MORRIS, P. J. & FISHER, M. J. 1979 Measurements in subsonic and supersonic free jets using a laser velocimeter. *J. Fluid Mech.* **93**, 1–27.

LOVE, E. S. 1959 Experimental and theoretical studies of axisymmetric free jets. *NASA TR*-R6.

NAYFEH, A. H. 1973 *Perturbation Methods*. Wiley-Interscience.

NORUM, T. D. & SEINER, J. M. 1982*a* Broadband shock noise from supersonic jets. *AIAA J.* **20**, 68–73.

NORUM, T. D. & SEINER, J. M. 1982*b* Measurements of mean static pressure and far field acoustics of shock-containing supersonic jets. *NASA TM* 84521.

PACK, D. C. 1950 A note on Prandtl's formula for the wavelength of a supersonic gas jet. *Q. J. Mech. Appl. Maths* **3**, 173–181.

PRANDTL, L. 1904 Über die stationären Wellen in einem Gasstrahl. *Phys. Zeit.* **5**, 599–601.

SALAS, M. D. 1974 The numerical calculation of inviscid plume flow fields. *AIAA paper no.* 74-523.

SCHLICHTING, H. 1960 *Boundary layer theory*. McGraw-Hill.

SEINER, J. M., DASH, S. M. & WOLF, D. E. 1983 Shock noise features using the SCIPVIS code. *AIAA paper no.* 83-0705.

SEINER, J. M. & NORUM, T. D. 1979 Experiments of shock associated noise on supersonic jets. *AIAA paper no.* 79-1526.

SEINER, J. M. & NORUM, T. D. 1980 Aerodynamic aspects of shock containing jet plumes. *AIAA paper no.* 80-0965.

SEINER, J. M. & YU, J. E. 1981 Acoustic near field and local flow properties associated with broadband shock noise. *AIAA paper no.* 81-1975.

TAM, C. K. W. 1972 On the noise of a nearly ideally expanded supersonic jet. *J. Fluid Mech.* **51**, 69–95.

TAM, C. K. W. 1975 Supersonic jet noise generated by large scale disturbances. *J. Sound Vib.* **38**, 51–79.

TAM, C. K. W. & TANNA, H. K. 1982 Shock associated noise of supersonic jets from convergent–divergent nozzles. *J. Sound Vib.* **81**, 337–358.